J. Fluid Mech. (2025), *vol.* 1017, A25, doi:10.1017/jfm.2025.10472

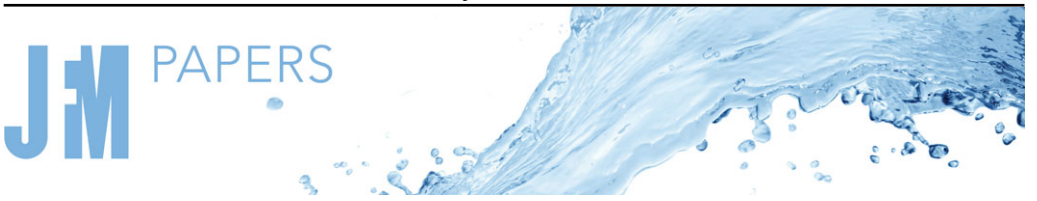

Radial flow of shear-thinning fluids: theoretical results, simulations and comparison with experiments

Amit Ashkenazi[1] **and Evgeniy Boyko**[1]

[1]Faculty of Mechanical Engineering, Technion – Israel Institute of Technology, Haifa 3200003, Israel

Corresponding author: Evgeniy Boyko, evgboyko@technion.ac.il

(Received 18 February 2025; revised 2 June 2025; accepted 10 July 2025)

We analyse the pressure-driven radial flow of a shear-thinning fluid between two parallel plates. Complex fluid rheology may significantly affect the hydrodynamic features of such non-Newtonian flows, which remain not fully understood, compared with Newtonian flows. We describe the shear-thinning rheology using the Ellis model and present a theoretical framework for calculating the pressure distribution and the flow rate–pressure drop relation. We first derive a closed-form expression for the pressure gradient, which allows us to obtain semi-analytical expressions for the pressure, velocity and flow rate–pressure drop relation. Specifically, we provide the corresponding asymptotic solutions for small and large values of the dimensionless flow rates. We further elucidate the entrance length required for the radial velocity of a shear-thinning fluid to reach its fully developed form, showing that this length approximates the Newtonian low-Reynolds-number value at low shear rates, but may strongly depend on the fluid's shear-thinning rheology and exceed the Newtonian value at high shear rates. We validate our theoretical results with finite-element numerical simulations and find excellent agreement. Furthermore, we compare our semi-analytical, asymptotic and finite-element simulation results for the pressure distribution with the experimental measurements of Laurencena & Williams (*Trans. Soc. Rheol.* vol. 18, 1974, pp. 331–355), showing good agreement. Our theoretical results using the Ellis model capture the interplay between the shear-thinning and the zero-shear-rate effects on the pressure drop, which cannot be explained using a simple power-law model, highlighting the importance of using an adequate constitutive model to accurately describe non-Newtonian flows of shear-thinning fluids.

Key words: non-Newtonian flows, rheology, lubrication theory

1. Introduction

Pressure-driven radial flows of non-Newtonian fluids are commonly encountered in industrial polymer processes, such as injection moulding and extrusion (Middleman 1977; Pearson 1985; Tadmor & Gogos 2013). It is well known that complex rheological characteristics of non-Newtonian fluids, such as shear thinning and viscoelasticity (Bird, Armstrong & Hassager 1987; Datta *et al.* 2022; Ewoldt & Saengow 2022), may significantly change their hydrodynamic features compared with Newtonian flows even at low Reynolds numbers. Therefore, understanding the impact of fluid rheology on the hydrodynamic features of complex fluid flows plays a fundamental role in non-Newtonian fluid mechanics.

A typical set-up commonly used to study the pressure-driven radial flow of non-Newtonian fluids is shown schematically in figure 1. This configuration consists of two parallel plates of radius r_o separated by a small gap h. The fluid is driven by a constant volumetric flow rate q through a narrow tube of radius r_i at the centre of the top plate. For such radial flows, it is of particular interest to understand how the complex fluid rheology affects the resulting flow field, pressure distribution $p(r)$, and pressure drop Δp between the inlet ($r = r_i$) and outlet ($r = r_o$) for a given flow rate q.

Over the years, different non-Newtonian fluids, characterised by various rheological behaviours, have been studied extensively in radial-flow configurations. Table 1 presents a chronological selection of previous work, clearly showing that earlier theoretical, numerical and experimental studies have considered the influence of shear-thinning, viscoelastic and viscoplastic rheology on radial flow behaviour.

The early theoretical studies on the radial flow of non-Newtonian fluids considered shear-thinning rheology using the simple power-law and Sisko models (Na & Hansen 1967; Khader & Vachon 1973). However, both power-law and Sisko models are too simplistic and cannot accurately describe the shear rate variation of viscosity of common non-Newtonian fluids over the entire range of shear rates. Specifically, these models do not replicate the low-shear-rate viscosity plateau and have a well-known singularity at zero shear rate (Bird *et al.* 1987). The Sisko model (Sisko 1958) reproduces the high-shear-rate viscosity plateau, but behaves similarly to the power-law model at low shear rates (Partal *et al.* 1994). To address the limitations of the power-law and Sisko models, Co (1981) solved numerically the radial flow of a shear-thinning fluid using a Carreau model (Carreau 1972), neglecting the high-shear-rate viscosity plateau. Unfortunately, Co (1981) considered the radial flow problem only within the power-law regime, and thus, as expected, their numerical results for velocity profile and pressure distribution showed good agreement with theoretical predictions based on the power-law model (Na & Hansen 1967). In this work, we consider the Ellis model (Reiner 1960; Matsuhisa & Bird 1965; Bird *et al.* 1987) to describe the shear-thinning rheology and show that, at low shear rates, the pressure distribution and pressure drop significantly differ from the power-law regime.

In the context of radial flows of shear-thinning fluids, it is worth mentioning recent studies on the instability of radially spreading extensional flows of shear-thinning fluids (Sayag & Worster 2019*a*,*b*; Hutchinson & Worster 2025). Instead of applying no-slip boundary conditions that lead to shear-dominated flows, Sayag & Worster (2019*b*) and Hutchinson & Worster (2025) used free-slip conditions, resulting in extensional-dominated flows. Specifically, using a combination of experiments and lubrication theory in conjunction with the power-law model, these studies considered the situation when the shear-thinning fluid displaces less viscous fluid in extensionally dominated flows.

Beyond shear-thinning fluids, radial flows of viscoelastic and viscoplastic fluids have also received much attention in the fluid mechanics and rheology communities

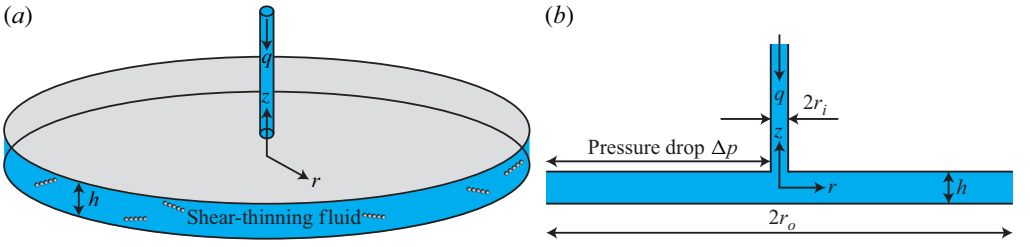

Figure 1. Schematic illustration of the flow configuration, showing the coordinate system and relevant physical parameters. (*a*) Radial flow of a shear-thinning fluid between two disk-shaped, parallel plates of radius r_o separated by a small gap h ($h \ll r_o$). The fluid is steadily driven by the imposed flow rate q through a narrow tube of radius r_i at the centre of the top plate. (*b*) Cross-section view of the geometry. Our interest is to determine the resulting pressure distribution and pressure drop Δp between the inlet ($r = r_i$) and outlet ($r = r_o$).

	Focus	Fluid/model	Comments
Na & Hansen (1967)	Theor.	Sisko, power law	
Schwarz & Bruce (1969)	Theor.	Third-order fluid	Weak viscoelastic effects
	Exptl.	Polyacrylamide solutions	
Khader & Vachon (1973)	Theor.	Power law	Included fluid inertia
Laurencena & Williams (1974)	Exptl.	Carbopol and Natrosol solutions	
Lee & Williams (1976*a*)	Theor.	Five-constant Oldroyd	Weak viscoelastic effects Included fluid inertia
Lee & Williams (1976*b*)	Exptl.	Polyacrylamide solutions	
Co & Bird (1977)	Theor.	Third-order fluid	Included fluid inertia Weak viscoelastic effects
Amadou *et al.* (1978)	Exptl.	Polyethylene oxide solutions	Converging radial flow
Dai & Bird (1981)	Theor.	Bingham	
Co (1981)	Numer.	Carreau	Neglected high-shear-rate viscosity plateau
Co & Stewart (1982)	Numer.	Modified Zaremba–Fromm–DeWitt	
Zou *et al.* (2020)	Theor./Numer.	Herschel–Bulkley	
Shamu *et al.* (2020)	Exptl.	Carbopol gels	
Albattat & Hoteit (2021)	Theor./Numer.	Herschel–Bulkley	
Present work	Theor./Numer.	Ellis	Comparison to experiments

Table 1. Chronological selection of previous theoretical, numerical and experimental studies on the pressure-driven radial flow of various complex, non-Newtonian fluids.

(see, e.g. Lee & Williams 1976*a*,*b*; Dai & Bird 1981; Co & Stewart 1982; Shamu *et al.* 2020; Zou, Håkansson & Cvetkovic 2020; Albattat & Hoteit 2021). Recently, Zou *et al.* (2020) studied the radial flow of viscoplastic fluids between homogeneous fractures and presented an analytical solution for the flow of the Herschel–Bulkley fluid model. In contrast to the modelling of the viscoplastic fluids, which allows considerable theoretical progress for a wide range of flow rates (Zou *et al.* 2020; Albattat & Hoteit 2021), all theoretical studies on viscoelastic fluids have considered to date only small Deborah or Weissenberg numbers, which correspond to weak viscoelasticity (Schwarz & Bruce 1969; Lee & Williams 1976*a*; Co & Bird 1977). Therefore, further investigation would be required to understand the radial flow of viscoelastic fluids at non-small Deborah/Weissenberg numbers; see the last paragraph of our conclusions in § 6.

In conjunction with theoretical and numerical investigations, experimental studies have been conducted on radial flows of various non-Newtonian fluids, including shear-thinning, viscoelastic and viscoplastic fluids (see, e.g. Schwarz & Bruce 1969; Laurencena & Williams 1974; Lee & Williams 1976*b*; Amadou, Adler & Piau 1978; Shamu *et al.* 2020). Of particular interest is an experimental study of Laurencena & Williams (1974) on the pressure-driven flow of non-Newtonian fluids. Laurencena & Williams (1974) measured the radial pressure distribution for three polymer solutions (two Carbopol solutions and one Natrosol solution). Using a power-law model for rheological characterisation and theoretical prediction for the pressure distribution (Na & Hansen 1967), Laurencena & Williams (1974) showed a quantitative comparison between theory and experiments. For the Natrosol solution, they found a good agreement between theory and experiments only for high flow rates, corresponding to the high shear rates, well captured by the power-law model. However, at low flow rates, which correspond to low shear rates, significant discrepancies existed between theoretical predictions and experimental results. Such discrepancy is due to the inability of the simple power-law model to accurately capture the rheological and hydrodynamic behaviours at low flow rates, as noted by Laurencena & Williams (1974) in their concluding remarks.

Indeed, while the power-law model is widely used because of its simplicity, it has certain limitations mentioned previously. Recent theoretical and numerical studies on the flow of shear-thinning fluids have demonstrated that the power-law model can reproduce the results of the more accurate Ellis and Carreau models only at intermediate shear rates (see, e.g. Moukhtari & Lecampion 2018; Boyko & Stone 2021*a*; Ciriello *et al.* 2021; Picchi *et al.* 2021; Longo *et al.* 2022; Barmak *et al.* 2024; Steinik *et al.* 2024). As a result, its range of applicability is quite limited, and caution should be taken when interpreting the results based on the power-law rheology at low and high shear rates.

In this work, we provide a theoretical framework for calculating the pressure distribution and the flow rate–pressure drop relation of a shear-thinning Ellis fluid in radial-flow configurations. The Ellis model exhibits a low-shear-rate viscosity plateau, consistent with the experimentally observed behaviour of shear-thinning fluids, and regularises the divergent behaviour of the power-law model at zero shear rate (Bird *et al.* 1987). Nevertheless, the Ellis model cannot reproduce the experimentally observed high-shear-rate viscosity plateau and predicts vanishing viscosity, similar to the power-law model. The experimentally observed viscosity plateau at high shear rates can be reproduced by more complex shear-thinning constitutive models, such as Cross (1965) and Carreau (1972), containing more fitting parameters than the Ellis model. However, the important feature and advantage of the Ellis model is that, unlike Carreau and Cross models, the Ellis model allows to obtain an explicit expression for the velocity profile in unidirectional, lubrication and thin-film flows (see, e.g. Gutfinger & Tallmadge 1965; Matsuhisa & Bird 1965; Steller 2001; Myers 2005; Ciriello *et al.* 2021; Picchi *et al.* 2021), thus making it useful for analytical analysis. As we show here, this fact allows us to obtain an explicit nonlinear equation that governs the pressure gradient in the radial flow of an Ellis fluid, suitable for both asymptotic and numerical investigations.

While our principal concern is the pressure distribution and the pressure drop driving the fluid, we also discuss the velocity profile of the Ellis fluid in a radial flow. To date, all theoretical studies on the radial flow of shear-thinning and viscoplastic fluids employing generalised Newtonian models, such as the power-law (Na & Hansen 1967; Laurencena & Williams 1974), Sisko (Na & Hansen 1967) and Herschel–Bulkley (Zou *et al.* 2020; Albattat & Hoteit 2021), have assumed the fully developed form of the radial velocity (see, e.g. Park 2020). However, the assumption of fully developed radial flow does not apply near the inlet, where fluid enters the gap between the plates from the tube.

Indeed, even for a Newtonian fluid at low Reynolds numbers, a radial entrance length is necessary to achieve a fully developed velocity profile (Chatterjee 1993, 2000). Thus, to provide insight into the validity of this assumption, we study over which length scale the radial velocity of the Ellis fluid reaches its fully developed form.

The paper is organised as follows. In § 2, we present the problem formulation, including governing equations, boundary conditions and the constitutive equation for the Ellis viscosity model. In § 3, we provide a closed-form expression for the non-dimensional pressure gradient, which allows us to obtain semi-analytical expressions for the pressure, velocity and pressure drop. Furthermore, we derive the corresponding asymptotic solutions for small and large values of the dimensionless flow rates. We present the results in § 4, including a comparison between our semi-analytical and asymptotic predictions and the finite-element numerical simulations, finding excellent agreement. We further use numerical simulations to study the entrance length required for the radial velocity of the Ellis fluid to achieve its fully developed form. In § 5, we compare the predictions of our theoretical and finite-element analyses with the experimental results of Laurencena & Williams (1974) for the pressure distribution of the Natrosol solution, showing good agreement. We conclude with a discussion of the results in § 6.

2. Problem formulation, governing equations and shear-thinning rheology

We study the steady, pressure-driven radial flow of a non-Newtonian shear-thinning fluid between two disk-shaped plates of radius r_o separated by a small gap h, where $h \ll r_o$. We assume that the incompressible and axisymmetric flow is driven by a constant volumetric flow rate q through a narrow tube of radius $r_i \ll r_o$, which feeds into the centre of the top plate, as shown in figure 1. The imposed flow rate q induces the radial fluid motion with velocity $\boldsymbol{u} = (u_r, u_z)$ and pressure distribution p. Motivated by the experiments of Laurencena & Williams (1974), we are interested in determining the resulting pressure distribution and pressure drop Δp between the inlet ($r = r_i$) and outlet ($r = r_o$) for a given q.

We consider low-Reynolds-number flows and neglect the fluid inertia. In this limit, the continuity and momentum equations governing the fluid motion take the form

$$\boldsymbol{\nabla} \cdot \boldsymbol{u} = 0, \qquad \boldsymbol{\nabla} \cdot \boldsymbol{\sigma} = \boldsymbol{0}, \tag{2.1a,b}$$

where $\boldsymbol{\sigma}$ is the stress tensor. The governing equations (2.1) are supplemented by the no-slip and no-penetration boundary conditions along the plates walls, $\boldsymbol{u} = \boldsymbol{0}$ at $z = \pm h/2$, and the integral constraint for the flow rate, $q = 2\pi \int_{-h/2}^{h/2} u_r r \, \mathrm{d}z$. In addition, for convenience, we set a zero gauge pressure at $r = r_o$, so that $p(r = r_o) = 0$.

We describe the shear-thinning rheology of the non-Newtonian fluid using a generalised Newtonian model, with stress tensor $\boldsymbol{\sigma}$ given by (Bird *et al.* 1987)

$$\boldsymbol{\sigma} = -p\boldsymbol{I} + \boldsymbol{\tau} = -p\boldsymbol{I} + 2\eta(\dot{\gamma})\boldsymbol{E}, \tag{2.2}$$

where $\boldsymbol{\tau}$ is the deviatoric stress tensor and $\boldsymbol{E} = (\boldsymbol{\nabla u} + (\boldsymbol{\nabla u})^{\mathrm{T}})/2$ is the rate-of-strain tensor. Similar to Newtonian fluids, the stress tensor $\boldsymbol{\sigma}$ of the generalised Newtonian fluids depends only on the instantaneous flow and not the flow history. Therefore, the generalised Newtonian constitutive model is inelastic and does not account for viscoelasticity. Nevertheless, in contrast to the Newtonian fluid, the viscosity η of the generalised Newtonian fluid depends on either the shear rate $\dot{\gamma} = \sqrt{2\boldsymbol{E} : \boldsymbol{E}}$, $\eta(\dot{\gamma})$, or the magnitude of the shear stress $\tau = \sqrt{(\boldsymbol{\tau} : \boldsymbol{\tau})/2}$, $\eta(\tau)$.

In this work, we are interested in understanding the interplay between the shear-thinning and the zero-shear-rate effects on the pressure drop in the radial flow. To this end,

we consider the Ellis model for the apparent viscosity, which provides the viscosity in terms of the shear stress and captures the experimentally observed viscosity behaviour at low shear rates and power-law dependence at intermediate shear rates. The constitutive equation for an Ellis viscosity model is given by (Reiner 1960; Matsuhisa & Bird 1965; Bird *et al.* 1987)

$$\text{Ellis model:} \qquad \eta(\tau) = \frac{\eta_0}{1 + (\tau/\tau_{1/2})^{n_e - 1}}, \tag{2.3}$$

where η_0 is the zero-shear-rate viscosity. The index n_e represents the degree of shear thinning, $n_e \geqslant 1$, and the constant $\tau_{1/2}$ controls the onset of the shear-thinning effect, representing the effective shear stress at which the viscosity is 50 % of the zero-shear-rate viscosity η_0. The case $\tau_{1/2} \to \infty$ represents the Newtonian fluid with a constant viscosity η_0, whereas the case $n_e = 1$ represents the Newtonian fluid with a constant viscosity $\eta_0/2$.

For low shear stresses (or shear rates), $\tau/\tau_{1/2} \ll 1$, the Ellis model exhibits a plateau with zero-shear-rate viscosity η_0, similar to the Carreau and Cross models, consistent with the experimentally observed behaviour of shear-thinning fluids. Thus, the Ellis model regularises the divergent behaviour of the power-law model as $\dot{\gamma} \to 0$. For intermediate and high stresses (or shear rates), $\tau/\tau_{1/2} \gg 1$, the Ellis model reduces to the power-law model (Picchi *et al.* 2021; Christov 2022)

$$\text{power-law model:} \qquad \eta(\dot{\gamma}) = m\dot{\gamma}^{n-1}, \quad \text{with } m = \eta_0^n \tau_{1/2}^{1-n} \text{ and } n = 1/n_e. \tag{2.4}$$

However, similar to the power-law model, the Ellis model cannot reproduce the experimentally observed high-shear-rate viscosity plateau and predicts vanishing viscosity as $\dot{\gamma} \to \infty$. We note that the Ellis model can be extended to account for the high-shear-rate viscosity plateau, resulting in the Meter model, given by $\eta(\tau) = \eta_\infty + (\eta_0 - \eta_\infty)/(1 + (\tau/\tau_m)^{n_e - 1})$ (Meter & Bird 1964; Shende, Niasar & Babaei 2021), where η_∞ is the infinite-shear-rate viscosity and τ_m is the effective shear stress at which the viscosity reaches 50 % of $\eta_0 + \eta_\infty$.

3. Theoretical analysis for the radial flow of a shear-thinning fluid

3.1. *Velocity and flow rate–pressure gradient relation in dimensional form*

We consider low-Reynolds-number flow of an incompressible shear-thinning fluid in a narrow configuration where $h \ll r_o$, which allows for the use of the lubrication approximation. Specifically, the lubrication approximation applies provided that the aspect ratio $\epsilon = h/r_o$ and the reduced Reynolds number ϵRe are small, i.e. $\epsilon \ll 1$ and $\epsilon Re \ll 1$ (Leal 2007).

The reduced Reynolds number ϵRe is the ratio of fluid inertia, $\rho u_c^2/r_o$, to viscous stress, $\eta(\dot{\gamma})u_c/h^2$, where $u_c = q/2\pi h r_o$ is the characteristic velocity scale and ρ is the density of the fluid. In contrast to a Newtonian fluid, where the reduced Reynolds number ϵRe depends linearly on velocity (or shear rate $\dot{\gamma} \sim u_c/h$), the reduced Reynolds number for a shear-thinning fluid may exhibit either linear or nonlinear dependence on velocity, depending on the magnitude of the shear rate or shear stress. For low shear stresses (or shear rates), $\tau/\tau_{1/2} \ll 1$, the viscosity of the Ellis fluid is $\eta(\dot{\gamma}) \approx \eta_0$, so that the small reduced Reynolds number assumption requires $\epsilon Re_{small\ El} = \rho u_c h^2/\eta_0 r_o \ll 1$, similar to a Newtonian fluid. However, for high shear stresses (or shear rates), $\tau/\tau_{1/2} \gg 1$, the viscosity of the Ellis fluid follows the power-law dependence (2.4) and is approximately $\eta(\dot{\gamma}) \approx \eta_0(\eta_0\dot{\gamma}/\tau_{1/2})^{(1/n_e)-1}$. Therefore, the small reduced Reynolds number assumption now requires that $\epsilon Re_{power\text{-}law} = (\rho u_c h^2/\eta_0 r_o)(\eta_0 u_c/h\tau_{1/2})^{1-(1/n_e)} \ll 1$, which can also be expressed as $\epsilon Re_{power\text{-}law} = (\epsilon Re_{small\ El}) El^{1-(1/n_e)} \ll 1$, where $El = \eta_0 u_c/h\tau_{1/2}$ is

the Ellis number defined in (3.10). As expected, in the power-law regime, the reduced Reynolds number increases nonlinearly with velocity (or the Ellis number) due to the shear-thinning behaviour of the fluid. Clearly, in the power-law regime where $El \gg 1$, the condition $\epsilon Re_{power\text{-}law} = (\epsilon Re_{small\ El}) El^{1-(1/n_e)} \ll 1$ is more restrictive than $\epsilon Re_{small\ El} \ll 1$, since the latter does not necessarily imply that $\epsilon Re_{power\text{-}law} \ll 1$. Nevertheless, for typical values of the physical parameters associated with the radial flow of an Ellis fluid, listed in table 4, both conditions, $\epsilon Re_{small\ El} \ll 1$ and $\epsilon Re_{power\text{-}law} \ll 1$, are well satisfied, as shown in Appendix C.

In this lubrication limit, fluid inertia and longitudinal gradients are negligible, and we can assume a unidirectional radial flow, $\boldsymbol{u} = u_r(r, z)\boldsymbol{e}_r$ (see, e.g. Park 2020). Under this assumption, the momentum equations (2.1*b*) in conjunction with (2.2) and (2.3) reduce to

$$\frac{\partial p}{\partial r} = \frac{\partial}{\partial z}\left(\eta(\tau)\frac{\partial u_r}{\partial z}\right), \qquad \frac{\partial p}{\partial z} = 0, \tag{3.1a,b}$$

where the magnitude of the shear stress $\tau = \sqrt{(\boldsymbol{\tau} : \boldsymbol{\tau})/2}$ is given by

$$\tau = |\tau_{rz}| = \eta(\tau)\dot{\gamma} \quad \text{with } \dot{\gamma} = \left|\frac{\partial u_r}{\partial z}\right|. \tag{3.2}$$

The governing equations (3.1) represent the lubrication equations that can be derived by introducing a small parameter $\epsilon = h/r_o \ll 1$, and then formally expanding the velocity and pressure fields in powers of ϵ and considering the leading order terms (see, e.g. Oron, Davis & Bankoff 1997; Leal 2007). From (3.1*b*), it follows that $p = p(r)$, i.e. the pressure is constant across the gap h, but varies along the r-direction.

Integrating (3.1*a*) with respect to z and applying the symmetry condition at $z = 0$ yields

$$\frac{\mathrm{d}p}{\mathrm{d}r} z = \eta(\tau)\frac{\partial u_r}{\partial z}. \tag{3.3}$$

Substituting (2.3) into (3.3) and rearranging, we obtain

$$\frac{\partial u_r}{\partial z} = \frac{\mathrm{d}p}{\mathrm{d}r}\frac{z}{\eta(\tau)} = \frac{1}{\eta_0}\frac{\mathrm{d}p}{\mathrm{d}r} z(1 + (\tau/\tau_{1/2})^{n_e-1}). \tag{3.4}$$

Noting that $\dot{\gamma} = -\partial u_r/\partial z$ for $0 \leqslant z \leqslant h/2$, and using (3.2) and (3.3), the magnitude of the shear stress τ can be expressed as

$$\tau = -\eta(\tau)\frac{\partial u_r}{\partial z} = -\frac{\mathrm{d}p}{\mathrm{d}r} z \quad \text{for} \quad 0 \leqslant z \leqslant h/2, \tag{3.5}$$

where we expect the pressure gradient to be negative, $\mathrm{d}p/\mathrm{d}r < 0$.

Combining (3.4) and (3.5) provides the expression for $\partial u_r/\partial z$. Integrating this result with respect to z and applying the no-slip boundary conditions at the plate walls, we obtain an explicit expression for the radial velocity profile of an Ellis fluid,

$$u_r(r, z) = \frac{1}{\eta_0}\frac{\mathrm{d}p}{\mathrm{d}r}\left[\frac{1}{2}\left(z^2 - \frac{h^2}{4}\right) + \frac{1}{n_e + 1}\left(-\frac{\mathrm{d}p}{\mathrm{d}r}\frac{1}{\tau_{1/2}}\right)^{n_e-1}\left(z^{n_e+1} - \frac{h^{n_e+1}}{2^{n_e+1}}\right)\right]. \tag{3.6}$$

Finally, substituting (3.6) into the integral constraint for the volumetric flux, $q = 2\pi \int_{-h/2}^{h/2} u_r r \, \mathrm{d}z$ provides a nonlinear equation for the pressure gradient $\mathrm{d}p(r)/\mathrm{d}r$ for a given flow rate q,

$$\frac{q}{4\pi r} = -\frac{1}{\eta_0}\frac{\mathrm{d}p}{\mathrm{d}r}\left[\frac{h^3}{24} + \frac{h^{n_e+2}}{2^{n_e+2}(n_e + 2)}\left(-\frac{\mathrm{d}p}{\mathrm{d}r}\frac{1}{\tau_{1/2}}\right)^{n_e-1}\right]. \tag{3.7}$$

In addition, the integral constraint for the volumetric flux, $q = 2\pi \int_{-h/2}^{h/2} u_r r \, \mathrm{d}z$, implies that the radial velocity has the fully developed form of $u_r(r, z) = f(z)/r$ (see, e.g. Park 2020). We will return to this point in § 4.

3.2. *Non-dimensionalisation*

To non-dimensionalise our hydrodynamic problem, we introduce dimensionless variables based on the lubrication theory,

$$R = \frac{r}{r_o}, \quad Z = \frac{z}{h}, \quad U_r = \frac{u_r}{u_c}, \quad P = \frac{p}{\eta_0 u_c r_o / h^2}, \quad \Delta P = \frac{\Delta p}{\eta_0 u_c r_o / h^2}, \quad \mathcal{H} = \frac{\eta}{\eta_0}, \tag{3.8}$$

where $u_c = q/2\pi h r_o$ is the characteristic velocity scale. In addition, we introduce the inlet-to-outlet aspect ratio $\alpha = r_i/r_o$, which is assumed to be small, $\alpha \ll 1$, consistent with the experiments of Laurencena & Williams (1974).

Using the non-dimensionalisation (3.8), the governing equation for the pressure gradient (3.7) takes the form

$$\frac{1}{R} = -\frac{\mathrm{d}P}{\mathrm{d}R}\left[\frac{1}{12} + \frac{1}{2^{n_e+1}(n_e+2)}\left(-El\frac{\mathrm{d}P}{\mathrm{d}R}\right)^{n_e-1}\right], \tag{3.9}$$

where El is the non-dimensional Ellis number defined as

$$El = \frac{\dot{\gamma}_c}{\tau_{1/2}/\eta_0} = \frac{\eta_0 u_c}{h\tau_{1/2}} = \frac{\eta_0 q}{2\pi h^2 r_o \tau_{1/2}}. \tag{3.10}$$

The Ellis number is the ratio of the characteristic shear rate in the flow, $\dot{\gamma}_c = u_c/h$, to the cross-over shear rate of the fluid, $\tau_{1/2}/\eta_0$, representing the relative importance of the shear thinning. For $El \ll 1$, the onset of shear-thinning effect occurs only at sufficiently high shear rates, and the fluid is expected to behave as Newtonian. In contrast, when $El \gg 1$, we expect the shear-thinning effect to become apparent at low shear rates, and the shear-thinning fluid follows the power-law model. We note that the definition of the Ellis number, (3.10), is similar to the definition of the Carreau number, provided $\tau_{1/2} = \eta_0/\lambda$, where λ is the inverse of a characteristic shear rate of the Carreau fluid (see, e.g. Boyko & Stone 2021*b*; Chun *et al.* 2024). However, our definition of the Ellis number is inverse to the definition used in recent studies of Picchi *et al.* (2021) and Chun *et al.* (2022).

Using the non-dimensionalisation (3.8), the Ellis and power-law models, (2.3) and (2.4), can be expressed in the dimensionless form in terms of the Ellis number,

$$\mathcal{H}_{Ellis} = \frac{1}{1 + (\mathcal{H}_{Ellis} El)^{n_e-1}} \quad \text{and} \quad \mathcal{H}_{power\text{-}law} = El^{\frac{1}{n_e}-1}, \quad \text{with } El = \frac{\dot{\gamma}}{\tau_{1/2}/\eta_0}. \tag{3.11}$$

We present in figure 2 the dimensionless viscosity $\mathcal{H} = \eta/\eta_0$ as a function of the Ellis number $El = \eta_0\dot{\gamma}/\tau_{1/2}$ for $n_e = 1.5$, 2.5 and 5. As expected, for small values of El, we recover the Newtonian plateau with $\mathcal{H} = 1$, whereas for large values of El, we obtain the power-law behaviour with $\mathcal{H} = El^{(1/n_e)-1}$, represented by red dashed lines. It is evident that as the index n_e characterising the degree of shear thinning increases, the viscosity transitions from the small-El (Newtonian) to the power-law behaviour at smaller values of the Ellis number.

For arbitrary values of the Ellis number, the pressure gradient $\mathrm{d}P/\mathrm{d}R \equiv P'(R)$ can be calculated numerically from (3.9), as detailed in Appendix A. Once the pressure gradient $P'(R)$ is known, the pressure distribution $P(R)$ and pressure drop $\Delta P \equiv P(R = \alpha) - P(R = 1)$, expressed in terms of the integrals,

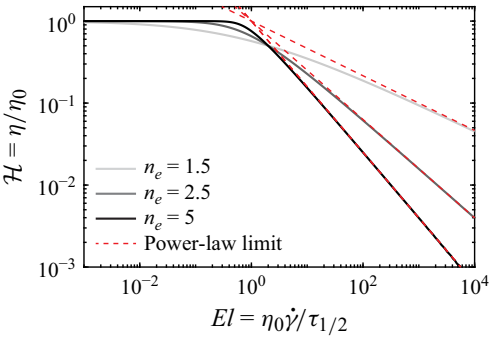

Figure 2. Non-dimensional viscosity $\mathcal{H} = \eta/\eta_0$ as a function of the Ellis number $El = \eta_0\dot{\gamma}/\tau_{1/2}$ for different values of the shear-thinning index n_e. Red dashed lines represent the power-law asymptotic limit valid for large values of El.

$$P(R) = -\int_R^1 P'(R)\,\mathrm{d}R \quad \text{and} \quad \Delta P = P(\alpha) = -\int_\alpha^1 P'(R)\mathrm{d}R, \tag{3.12a,b}$$

can be obtained using numerical integration (see Appendix A). Note that, in (3.12), we have used the fact that $P(1) = 0$.

Furthermore, having obtained the pressure gradient $\mathrm{d}P/\mathrm{d}R$, we can determine the non-dimensional radial velocity of an Ellis fluid using (3.6) as

$$U_r(R, Z) = \frac{\mathrm{d}P}{\mathrm{d}R}\left[\frac{1}{2}\left(Z^2 - \frac{1}{4}\right) + \frac{1}{n_e+1}\left(-El\frac{\mathrm{d}P}{\mathrm{d}R}\right)^{n_e-1}\left(Z^{n_e+1} - \frac{1}{2^{n_e+1}}\right)\right]. \tag{3.13}$$

3.3. *Asymptotic results for small and large values of Ellis number*

Although no closed-form analytical solution is available for (3.9), in this subsection, we provide asymptotic solutions in the limit of small and large values of El, thus allowing us to describe analytically almost the entire range of Ellis numbers.

For weak actuation, corresponding to the limit $El \ll 1$, we seek the solution for the pressure gradient $\mathrm{d}P/\mathrm{d}R \equiv P'(R)$ in the form

$$P'(R) = P_0'(R) + El^{n_e-1}P_1'(R) + El^{2(n_e-1)}P_2'(R) + O(El^{3(n_e-1)}). \tag{3.14}$$

Note that since $n_e \geqslant 1$, we have $El^{n_e-1} \ll 1$ and $El^{2(n_e-1)} \ll 1$ in the small-El limit. Substituting this expansion into (3.9) and solving order by order, we obtain

$$P_0'(R) = -\frac{12}{R}, \quad P_1'(R) = \frac{6^{n_e+1}}{n_e+2}\left(\frac{1}{R}\right)^{n_e}, \quad P_2'(R) = -\frac{3^{2n_e+1}4^{n_e}n_e}{(n_e+2)^2}\left(\frac{1}{R}\right)^{2n_e-1}. \tag{3.15}$$

Integrating (3.15) with respect to R and using the boundary condition $P(R=1) = 0$ provides the expression for the pressure,

$$P(R) = \underbrace{-12\ln R}_{P_0(R)} + El^{n_e-1}\underbrace{\frac{6^{n_e+1}}{(n_e+2)(n_e-1)}(1 - R^{1-n_e})}_{P_1(R)} + El^{2(n_e-1)}\underbrace{\frac{2^{2n_e-1}3^{2n_e+1}n_e}{(n_e+2)^2(n_e-1)}(R^{2-2n_e} - 1)}_{P_2(R)} \quad \text{for } El \ll 1. \tag{3.16}$$

Thus, the pressure drop ΔP in the small-El limit is

$$\Delta P = \underbrace{-12\ln\alpha}_{\Delta P_0} + El^{n_e-1}\underbrace{\frac{6^{n_e+1}}{(n_e+2)(n_e-1)}(1-\alpha^{1-n_e})}_{\Delta P_1} + El^{2(n_e-1)}\underbrace{\frac{2^{2n_e-1}3^{2n_e+1}n_e}{(n_e+2)^2(n_e-1)}(\alpha^{2-2n_e}-1)}_{\Delta P_2} \quad \text{for } El \ll 1. \tag{3.17}$$

For strong actuation, corresponding to the limit of $El \gg 1$, the Ellis model reduces to the power-law model and we expect to achieve a power-law regime. Specifically, the first term in the brackets on the right-hand side of (3.9) is negligible compared with the second term, so that the pressure gradient $P'(R)$ can be expressed as

$$P'(R) = -2^{(n_e+1)/n_e}(n_e+2)^{1/n_e}\frac{El^{(1-n_e)/n_e}}{R^{1/n_e}} \quad \text{for } El \gg 1. \tag{3.18}$$

Integrating (3.18) with respect to R and using the boundary condition $P(R=1)=0$ yields the expression for the pressure in the large-Ellis-number limit

$$P(R) = -\frac{2^{(n_e+1)/n_e}n_e(n_e+2)^{1/n_e}}{n_e-1}El^{(1-n_e)/n_e}(R^{(n_e-1)/n_e}-1) \quad \text{for } El \gg 1, \tag{3.19}$$

so that the pressure drop in the large-El limit is

$$\Delta P = -\frac{2^{(n_e+1)/n_e}n_e(n_e+2)^{1/n_e}}{n_e-1}El^{(1-n_e)/n_e}(\alpha^{(n_e-1)/n_e}-1) \quad \text{for } El \gg 1. \tag{3.20}$$

We note that, as expected, (3.20), when written in a dimensional form, agrees with the expression for the pressure drop of the power-law fluid (see, e.g. Na & Hansen 1967; Laurencena & Williams 1974). Furthermore, for $n_e = 1$, (3.20) reduces to $\Delta P = -12\ln\alpha$, consistent with the Newtonian limit.

4. Theoretical predictions and comparison with finite-element simulations

In this section, we present the theoretical and asymptotic results obtained in § 3. In addition, we validate the predictions of our theoretical model against the two-dimensional numerical simulations with the finite-element software COMSOL Multiphysics. The details of the numerical procedure are provided in Appendix B. The values of the physical parameters used in the finite-element simulations are summarised in table 4. We note that the fluid inertia is negligible in our simulations since the reduced Reynolds number is vanishingly small, as shown and discussed in Appendix C.

4.1. *Pressure drop and pressure distribution*

First, in figure 3(*a*,*b*), we present the non-dimensional pressure drop $\Delta P = \Delta p/(\eta_0 q/2\pi h^3)$ as a function of El for the radial flow of an Ellis fluid for $n_e = 1.5$ in panel (*a*) and $n_e = 2.5$ in panel (*b*), with $\alpha = 0.05$. Black triangles represent the finite-element simulation results obtained from calculating the pressure drop along the midplane $Z = 0$. Grey circles represent the theoretical results obtained by solving numerically (3.9) and (3.12*b*). Cyan dotted and red dashed curves represent the asymptotic solutions (3.17) and (3.20) for small and large values of El, respectively. Clearly, there is excellent agreement between the theoretical predictions based on our reduced-order model and finite-element

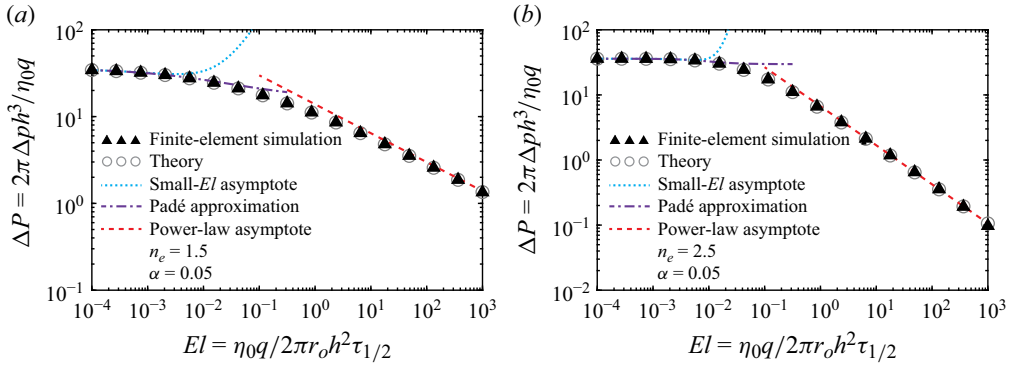

Figure 3. Non-dimensional pressure drop of the shear-thinning Ellis fluid in a radial flow between two disk-shaped plates. (*a*,*b*) Dimensionless pressure drop $\Delta P = \Delta p/(\eta_0 q/2\pi h^3)$ as a function of $El = \eta_0 q/(2\pi h^2 r_o \tau_{1/2})$ for (*a*) $n_e = 1.5$ and (*b*) $n_e = 2.5$. Black triangles represent the results of the finite-element simulation. Grey circles represent the theoretical results obtained by solving numerically (3.9) and (3.12*b*). Cyan dotted curves represent the small-El asymptotic solution (3.17). Purple dash-dotted curves represent the Padé approximation (4.1). Red dashed lines represent the power-law asymptotic solution (3.20). All calculations were performed using $\alpha = 0.05$.

simulation results. We observe that, as expected, the power-law asymptotic solution (3.20) captures fairly well the variation of the pressure drop with El for large values of the Ellis number. However, the small-El asymptotic solution (3.17) cannot accurately capture the pressure drop except for very small values of El. Nevertheless, using small-El asymptotic expressions for ΔP_0, ΔP_1 and ΔP_2 given in (3.17), we can improve the convergence of the asymptotic series by applying the diagonal Padé [1/1] approximation (Hinch 1991; Housiadas 2017),

$$\Delta P_{Pade} = \Delta P_0 + El^{n_e-1}\frac{(\Delta P_1)^2}{\Delta P_1 - El^{n_e-1}\Delta P_2} \quad \text{for } El \ll 1, \tag{4.1}$$

represented in figure 3(*a*,*b*) by purple dash-dotted curves.

It is evident from figure 3(*a*,*b*) that the Padé approximation (4.1) significantly improves the agreement with the semi-analytical and finite-element simulation results for both $n_e = 1.5$ and 2.5. For example, in the case of $n_e = 1.5$, we have a modest relative error of approximately 8 % for up to $El = 0.04$. As expected, when El increases, the agreement between the Padé approximation (4.1) and simulations deteriorates, and the small-El Padé approximation overpredicts the pressure drop, yielding a relative error of approximately 18 % for $El = 0.115$. Nevertheless, our theoretical predictions based on (3.9) and (3.12*b*) are in excellent agreement with simulations even for order-one Ellis numbers, resulting in a relative error below 0.5 % for $El = 0.87$ and $n_e = 1.5$. Therefore, our theory accurately describes the pressure drop behaviour and captures well the transition to the power-law dependence $\Delta P \sim El^{(1/n_e)-1}$, given in (3.20), for larger values of El. The dimensionless pressure drop, which physically represents the dimensionless flow resistance $(\Delta p/q)$ of the Ellis fluid, monotonically decreases with El. Interestingly, for $El \gg 1$, the scaling for the pressure $\Delta P \sim El^{(1/n_e)-1}$ is identical to the power-law dependence of the dimensionless viscosity $\mathcal{H} = El^{(1/n_e)-1}$, thus highlighting that the pressure drop reduction for shear-thinning fluids is due to the decrease in viscosity η with the applied shear rate $\dot{\gamma}$ or the shear stress τ.

Next, we present in figure 4(*a*,*b*) the non-dimensional pressure distribution $P = 2\pi p h^3/(\eta_0 q)$ as a function of the radial coordinate $R = r/r_o$ for the radial flow of an Ellis fluid for $n_e = 1.5$ in panel (*a*) and $n_e = 2.5$ in panel (*b*), with $El = 0.05$ and

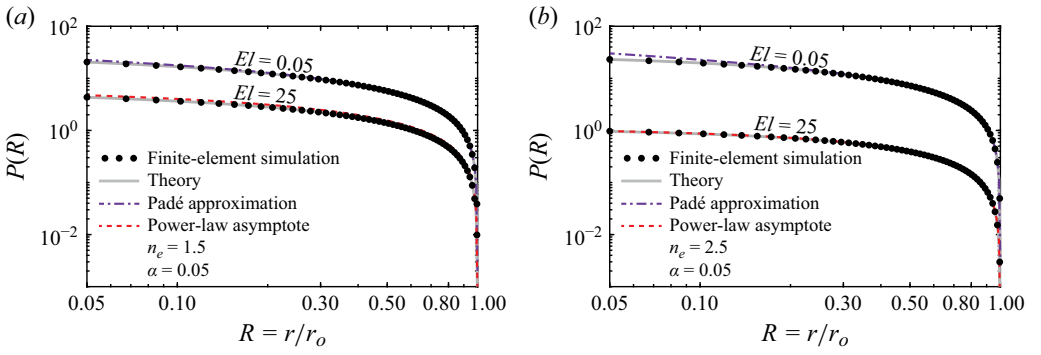

Figure 4. Non-dimensional pressure distribution of the shear-thinning Ellis fluid in a radial flow between two disk-shaped plates. (*a*,*b*) Dimensionless pressure $P = 2\pi ph^3/(\eta_0 q)$ as a function of the radial coordinate $R = r/r_o$ for small ($El = 0.05$) and large ($El = 25$) Ellis numbers with (*a*) $n_e = 1.5$ and (*b*) $n_e = 2.5$. Black dots represent the results of the finite-element simulation. Grey curves represent the theoretical results obtained by solving numerically (3.9) and (3.12*a*). Purple dash-dotted curves represent the small-El Padé approximation based on (3.16). Red dashed curves represent the power-law asymptotic solution (3.19). All calculations were performed using $\alpha = 0.05$.

$El = 25$. Similar to the pressure drop, our theoretical predictions for the pressure (grey solid curves) accurately capture the finite-element simulation results (black dots) for all considered values of El. Furthermore, we observe an excellent agreement between the small- and large-El asymptotic solutions (purple dash-dotted and red dashed curves) and the finite-element simulation results. Note that the small-El asymptotic solution is based on the application of the Padé approximation to the expressions in (3.16), similar to (4.1).

As expected, the results in figure 4(*a*,*b*) reveal that, for $El \ll 1$, the pressure distribution shows a weak dependence on the shear-thinning index n_e. However, for $El \gg 1$, the pressure magnitude decreases as n_e increases, consistent with the results shown in figure 2, indicating that the viscosity reduction for a given El in the power-law regime becomes more pronounced with n_e.

4.2. *Comparison between the theoretical predictions and the finite-element simulations for the radial velocity*

Our theoretical analysis presented in § 3 relies on the assumption of a unidirectional radial flow, $\boldsymbol{U} = U_r(R, Z)\boldsymbol{e}_r$, which together with the integral constraint for the volumetric flux, $\int_{-1/2}^{1/2} U_r R \, \mathrm{d}Z = 1$, implies that the radial velocity takes the fully developed form of $U_r(R, Z) = \mathcal{F}(Z)/R$ for $\alpha \leqslant R \leqslant 1$ (see, e.g. Na & Hansen 1967; Park 2020). Clearly, the assumption of unidirectional radial flow is not valid near the inlet, where the shear-thinning fluid enters from the tube into the gap between the plates. Indeed, even for a Newtonian fluid at low Reynolds numbers, there is a radial entrance length required to reach a fully developed velocity profile $U_r(R, Z) = -(3/2R)(4Z^2 - 1)$ (Chatterjee 1993, 2000). Therefore, it is of particular interest to compare our theoretical predictions for the radial velocity of the shear-thinning Ellis fluid with the results of the numerical simulations and elucidate over which length scale the radial velocity reaches its fully developed form, $U_r(R, Z) = \mathcal{F}(Z)/R$.

In figure 5, we present the results of the dimensionless radial velocity of the shear-thinning Ellis fluid in a radial flow for $n_e = 2.5$ and the Ellis number $El = 0.1$, corresponding to the transition from the small-El limit to the power-law regime, as shown in figure 3(*b*). Figure 5(*a–d*) shows a comparison of theoretical predictions

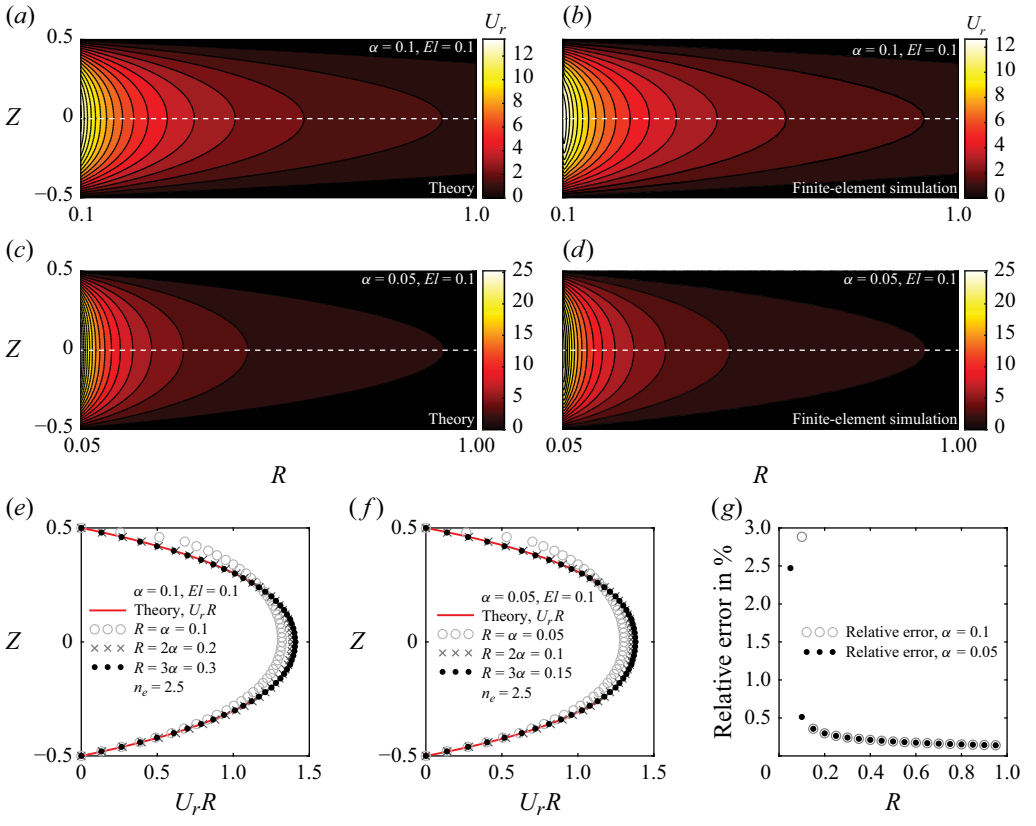

Figure 5. Non-dimensional radial velocity distribution of the shear-thinning Ellis fluid in a radial flow between two disk-shaped plates. (*a–d*) Contour plot of the radial velocity distribution, U_r, as a function of the (R, Z) coordinates for (*a*,*b*) $\alpha = 0.1$ and (*c*,*d*) $\alpha = 0.05$, obtained from (*a*,*c*) our theory and (*b*,*d*) finite-element simulations. White dashed lines represent the midplane $Z = 0$. (*e*,*f*) Radial velocity U_r multiplied by the radial coordinate R, $U_r R$, as a function of Z for $R = \alpha$, 2α and 3α, with (*e*) $\alpha = 0.1$ and (*f*) $\alpha = 0.05$. Red solid lines represent the theoretical results obtained by solving (3.9) and (3.13). Dots, crosses and circles represent the results of the finite-element simulation. (*g*) Relative error between the theory and numerical simulations for the radial velocity along the midplane, $U_r(R, Z = 0)$, as a function of the radial coordinate R for $\alpha = 0.1$ (grey circles) and $\alpha = 0.05$ (black dots). All calculations were performed using $El = 0.1$ and $n_e = 2.5$.

(figures 5*a* and 5*c*) and finite-element simulation results (figures 5*b* and 5*d*) for contours of the radial velocity, U_r, as a function of the (R, Z) coordinates for the Ellis fluid with $\alpha = 0.1$ in panel (*a*,*b*) and $\alpha = 0.05$ in panel (*c*,*d*). We observe a very good agreement between the theoretical and numerical results for the radial velocity U_z for both $\alpha = 0.1$ and $\alpha = 0.05$ in the entire domain. However, as expected, near the inlet, the agreement deteriorates and for $\alpha = 0.1$, we see that the theoretically predicted radial velocity slightly overpredicts the magnitude of $U_r(R = \alpha, Z = 0)$ obtained from the simulation results.

To understand how fast the radial velocity attains its fully developed form, $U_r(R, Z) = \mathcal{F}(Z)/R$, we present in figure 5(*e*,*f*) the scaled radial velocity $U_r R$ as a function of Z for $R = \alpha$, 2α and 3α, with $\alpha = 0.1$ in panel (*e*) and $\alpha = 0.05$ in panel (*f*). Red solid lines represent our theoretical predictions, and dots, crosses and circles represent the finite-element simulation results. It is evident that the radial velocity at $R = \alpha$ (grey circles) is not symmetric with respect to the midplane $Z = 0$ and deviates from the theoretically predicted fully developed profile due to the entering fluid flow from the

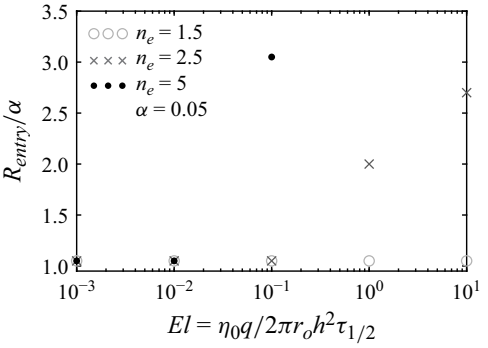

Figure 6. Radial entrance length R_{entry}, defined as the radial position R where the relative error between the theory and numerical simulations for the radial velocity along the midplane, $|(U_r^{theory} - U_r^{sim})/U_r^{sim}|_{Z=0}$, falls below 1 %, as a function of El for three values of the shear-thinning indices $n_e = 1.5$, 2.5 and 5. All calculations were performed using $\alpha = 0.05$.

tube into the gap between the plates. However, already at $R = 2\alpha$, we observe that the radial velocity becomes symmetric and our theory captures well the velocity profile for both $\alpha = 0.1$ and $\alpha = 0.05$. For further clarification, figure 5(*g*) presents the relative error between the theory and numerical simulations for the radial velocity along the midplane, $U_r(R, Z = 0)$, as a function of the radial coordinate R for $\alpha = 0.1$ (grey circles) and $\alpha = 0.05$ (black dots). It follows from figure 5(*g*) that the relative error, defined as $|(U_r^{theory} - U_r^{sim})/U_r^{sim}|_{Z=0}$, decays very fast and, for both $\alpha = 0.1$ and $\alpha = 0.05$, it is below 0.5 % when $R \gtrsim 0.105$.

So far, in figure 5, we have presented results for the radial velocity of a shear-thinning Ellis fluid with $El = 0.1$ and $n_e = 2.5$. To elucidate the influence of the Ellis number and the shear-thinning index on the development of the radial velocity, we present in figure 6 the radial entrance length R_{entry} (scaled by $\alpha = 0.05$), defined as the radial position R where the relative error $|(U_r^{theory} - U_r^{sim})/U_r^{sim}|_{Z=0}$ falls below 1 %, as a function of El for three different values of the shear-thinning indices $n_e = 1.5$, 2.5 and 5. We observe that for $El \ll 1$, the entrance length is independent of the shear-thinning index n_e and has a constant value of $R_{entry}/\alpha = 1.05$. However, as the Ellis number increases, the entrance length R_{entry} exhibits a strong dependence on n_e. While for $n_e = 1.5$, the entrance length remains nearly constant throughout the investigated range of Ellis numbers, for higher shear-thinning indices, the entrance length R_{entry} starts to increase with El above a certain value of the Ellis number, as observed for $n_e = 2.5$ and $n_e = 5$.

We note that our small-El results for the shear-thinning Ellis fluid are consistent with the previous estimate for the radial entrance length R_{entry} of a Newtonian fluid at low Reynolds numbers. Specifically, Chatterjee (2000) studied the radial entrance flow of a Newtonian fluid, considering a semi-infinite configuration in the radial direction, and defined the entrance length R_{entry} as the value of R at which the midplane radial velocity $U_r(R, Z = 0)$ is at 1 % from its fully developed value. In particular, Chatterjee (2000) found that $R_{entry} = 1.05\alpha$ for $h/r_i = 0.25$ in the absence of inertia. In our finite-element simulations, we have $\epsilon = 0.01$ and for $\alpha = 0.05$, we find that $R_{entry} \approx 1.05\alpha = 0.0525$ for $\epsilon/\alpha = h/r_i = 0.2$ and $El \leqslant 10^{-2}$, in close agreement with the Newtonian value of Chatterjee (2000).

To better understand the variation of the entrance length R_{entry} with the Ellis number and the shear-thinning index, we present in figure 7(*a*) the scaled radial velocity $U_r R$, evaluated at $(R, Z) = (0.1, 0)$, as a function of El for three different values of the shear-thinning

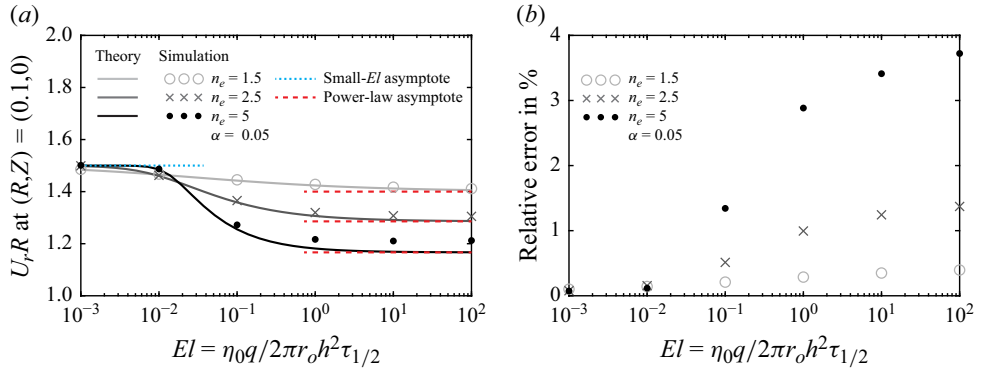

Figure 7. (*a*) Radial velocity U_r multiplied by the radial coordinate R, evaluated at $(R, Z) = (0.1, 0)$, as a function of El for three values of the shear-thinning indices $n_e = 1.5$, 2.5, and 5. Solid lines represent the theoretical results obtained by solving (3.9) and (3.13). Dots, crosses and circles represent the results of the finite-element simulation. The cyan dotted line represents the small-El asymptotic solution (4.2). Red dashed lines represent the power-law asymptotic solution (4.3). (*b*) Relative error between the theory and numerical simulations for the radial velocity at $(R, Z) = (0.1, 0)$ as a function of El for three values of the shear-thinning indices $n_e = 1.5$, 2.5 and 5. All calculations were performed using $\alpha = 0.05$.

indices $n_e = 1.5$, 2.5 and 5. Solid lines represent the theoretical results obtained by solving (3.9) and (3.13). Dots, crosses and circles represent the results of the finite-element simulation. The cyan dotted line represents the small-El (Newtonian) asymptotic solution,

$$U_r(R, Z) = -\frac{6}{R}\left(Z^2 - \frac{1}{4}\right) \quad \text{for } El \ll 1, \tag{4.2}$$

and red dashed lines represent the power-law asymptotic solution,

$$U_r(R, Z) = -\frac{2^{n_e+1}(n_e+2)}{(n_e+1)R}\left(Z^{n_e+1} - \frac{1}{2^{n_e+1}}\right) \quad \text{for } El \gg 1, \tag{4.3}$$

obtained from substituting (3.18) into (3.13) while neglecting the first term in the brackets of (3.13).

It is evident from figure 7(*a*) that the radial velocity shows a weak dependence on El and n_e for small Ellis numbers, consistent with the small-El asymptotic solution (4.2). Furthermore, the radial velocity exhibits a weak dependence on El for large Ellis numbers, yet retains a dependence on n_e, in agreement with the power-law asymptotic solution (4.3). However, in the transitional range of Ellis numbers, from the small-El (Newtonian) regime to the power-law behaviour, the radial velocity depends on both the Ellis number and the shear-thinning index.

The weak dependence of U_r on El and n_e for small Ellis numbers rationalises the weak dependence of the entrance length R_{entry} on the fluid rheology for $El \ll 1$, as shown in figure 6. This is also highlighted in figure 7(*b*), which shows the relative error between the theoretical prediction and numerical simulations for the radial velocity at $(R, Z) = (0.1, 0)$ as a function of El for three different values of the shear-thinning indices $n_e = 1.5$, 2.5 and 5. Clearly, for $n_e = 1.5$ and $n_e = 2.5$, the relative error at $(R, Z) = (0.1, 0)$ remains below 1 % when $El \leqslant 0.1$, supporting the conclusion that the entrance length R_{entry} is smaller than 0.1 in this regime. However, for $n_e = 5$, the relative error exceeds 1 % when $El \geqslant 0.1$, indicating that the entrance length is greater than 0.1 in this case.

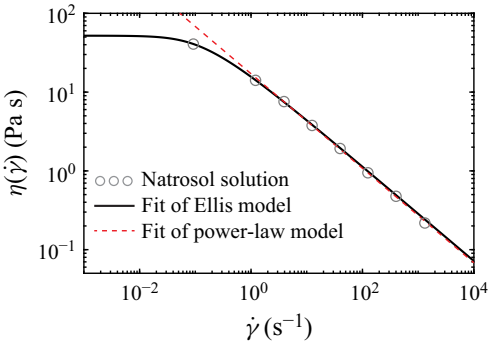

Figure 8. Experimental data from Laurencena & Williams (1974) and the fitting curves for viscosity as a function of shear rate for the Natrosol solution. The black curve represents the fit of the complete set of the rheological data (○) to the Ellis model (2.3). The red dashed curve represents the fit of the rheological data to the power-law model (2.4). The rheological parameters obtained from the fitting are summarised in table 2.

Rheological parameters	η_0 (Pa s)	$\tau_{1/2}$ (Pa)	n_e	n	m (Pa s^n)
Ellis model	52 ± 4	8.9 ± 1.5	2.5 ± 0.2	—	—
Power-law model	—	—	—	0.40 ± 0.01	17.1 ± 0.3
Power-law model (Laurencena & Williams 1974)	38.0	—	—	0.40	16.9

Table 2. Rheological parameters obtained from fitting the viscosity dependence on the shear rate of the Natrosol solution to the Ellis and power-law models based on the complete data set (upper row) and based solely on the data from the power-law regime (middle row). The lower row includes the fitting parameters reported by Laurencena & Williams (1974), who also determined η_0 using a falling ball viscometer at 21.5 °C. Certainty bounds are calculated based on the method presented by Ashkenazi & Solav (2025).

5. Comparison with experiments

In this section, we compare the predictions of our theoretical and finite-element analyses with the experimental results of Laurencena & Williams (1974), who measured the pressure distribution of the Natrosol solution in a radial flow between two disk-shaped plates for two different flow rates (see their figure 9). To this end, we first obtain the rheological parameters of the Ellis model.

5.1. *Fit of viscosity data and rheological parameters of the Ellis model*

Laurencena & Williams (1974) provided shear-rate-dependent viscosity data for the Natrosol solution measured with a Weissenberg rheogoniometer (see their figure 3). In addition, they used a falling ball viscometer to measure the zero-shear-rate viscosity η_0. We reproduce in figure 8 the viscosity data from Laurencena & Williams (1974) for the aqueous Natrosol solution, obtained using a Weissenberg rheogoniometer. The black curve represents the fit of the complete set of the rheological data to the Ellis model (2.3) obtained using MATLAB's nonlinear least-squares routine lsqcurvefit. The corresponding rheological parameters are provided in the upper row of table 2.

We observe that the leftmost data point in figure 8 corresponds to the transition from the low-shear-rate viscosity limit to the power-law regime. The red dashed curve represents the fit of the rheological data without this data point to the power-law model (2.4). The resulting rheological parameters, provided in the middle row of table 2, are in close agreement with the parameters from Laurencena & Williams (1974) for the power-law

	r_i (mm)	r_o (mm)	h (mm)	q (cm^3 s^{-1})	α	ϵ	El
Experiment 1	25.4	254	0.436	0.0121	0.1	1.72×10^{-3}	0.233
Experiment 2	25.4	254	0.914	6.01	0.1	3.60×10^{-3}	26.34

Table 3. Values of the physical parameters for the experimental system of Laurencena & Williams (1974), which measured the pressure distribution of the shear-thinning Natrosol solution as a function of the radial position for two different flow rates and heights. The values of El are calculated using η_0 and $\tau_{1/2}$ from the upper row of table 2, corresponding to fitting the viscosity dependence on the shear rate to the Ellis model.

regime, as given in the lower row. It follows from table 2 that $n \approx 1/n_e$, consistent with (2.4). While Laurencena & Williams (1974) used a falling ball viscometer to obtain the zero-shear-rate viscosity $\eta_0 = 38.0$ Pa s (see the lower row in table 2), unfortunately, they did not provide the error bars nor shear rate conditions for this measurement. Therefore, in our calculations, we use the value of η_0 obtained from the fitting to the Ellis model, which is a bit larger.

5.2. *A quantitative comparison between theory and experiments*

First, we summarise in table 3 the values of the physical parameters of the experimental system of Laurencena & Williams (1974) used for the measurements of the pressure distribution of the shear-thinning Natrosol solution as a function of the radial position for two different flow rates and heights. We observe that experimental values satisfy the lubrication assumptions of our theoretical analysis, $\epsilon = h/r_o \ll 1$.

Next, we present in figure 9(*a*,*b*) a comparison of our theoretical, asymptotic and finite-element simulation results with the experimental measurements of Laurencena & Williams (1974) for the pressure distribution of the shear-thinning Natrosol solution. Figure 9(*a*) represents the experiment 1 (the upper row in table 3), corresponding to $El = 0.233$, and figure 9(*b*) represents the experiment 2 (the lower row in table 3), corresponding to $El = 26.34$. Looking first at figure 9(*b*), we note the corresponding Ellis number $El = 26.34$ is within the power-law regime. In this case, we observe excellent agreement between our theoretical (grey curve) and finite-element simulation (black dots) predictions and the experimental results (grey circles). Furthermore, the power-law asymptotic solution (3.19) (red dashed curve) is indistinguishable from the full theoretical solution.

Figure 9(*a*) presents the pressure distribution as a function of the radial position for $El = 0.233$, corresponding to a transitional Ellis number from the small-El (Newtonian) to the power-law behaviour, consistent with the results shown in figures 2 and 3(*b*) for $n_e = 2.5$. First, there is good agreement between our theoretical predictions based on solving (3.9) and (3.12*a*) and the finite-element simulation results. However, neither the small-El Padé approximation nor the power-law asymptotic solution (3.19) can accurately capture the numerically predicted pressure variation at this transitional Ellis number, consistent with the results shown in figure 3(*b*).

Second, and more importantly, the experimental pressure distribution of the Natrosol solution, shown in figure 9(*a*), systematically overpredicts our theoretical and numerical results for $El = 0.233$, which are based on the inelastic shear-thinning Ellis model. We attribute this discrepancy to several factors. The first reason is the complex rheology of the non-Newtonian Natrosol solution, which is not a purely shear-thinning fluid but exhibits some elasticity, as reported by Laurencena & Williams (1974). While shear

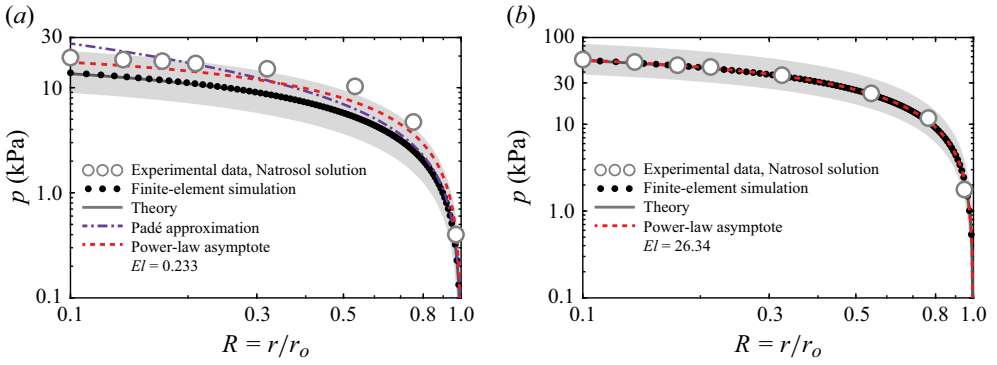

Figure 9. Comparison between our theory and the experimental data from Laurencena & Williams (1974) for the pressure distribution of the shear-thinning Natrosol solution in a radial flow between two disk-shaped plates. (*a*,*b*) Pressure p as a function of the radial coordinate $R = r/r_o$ for (*a*) experiment 1 and (*b*) experiment 2, whose details are summarised in table 3. Grey circles represent the experimental data, black dots represent the finite-element simulation results and grey curves represent the theoretical predictions. The purple dash-dotted curve represents the small-El Padé approximation based on (3.16) and red dashed curves represent the power-law asymptotic solution (3.19). The shaded regions indicate a 20 % uncertainty in the value of the gap h in the theoretical calculations due to the difficulties in measuring h in the experiments of Laurencena & Williams (1974).

thinning tends to decrease the pressure, fluid viscoelasticity has the opposite effect, increasing it. Therefore, the observed overprediction in figure 9(*a*) may be attributed to fluid viscoelasticity, which tends to increase the pressure. As noted by Co & Bird (1977), the net effect on pressure generally depends on the relative magnitudes of shear-thinning and viscoelasticity effects, provided that fluid inertia is negligible. Therefore, given the excellent agreement between theory and experiments in the power-law regime, as shown in figure 9(*b*), we expect the shear-thinning effect to dominate, while the effect of fluid elasticity is expected to be weak in this case. The second and major reason for the discrepancy is the uncertainty in the gap height h. Indeed, Laurencena & Williams (1974) reported the difficulties in accurately measuring h in the experiments due to a lack of rigidity in the support bearings. In experiment 1, shown in figure 9(*a*), the values of the flow rate q and height h are much smaller than in experiment 2, which we believe may increase uncertainty in the measured value of h. Therefore, we added a shaded region, based on taking a 20 % range from the reported experimental value of h. Clearly, we obtain a much better agreement between our theoretical and numerical predictions and the experimental results. We note that Laurencena & Williams (1974) did not provide the error bars for the pressure measurements, thus making it difficult to elucidate the error between the theory and experiments.

Finally, we note that, in addition to the pressure distribution measurements, Laurencena & Williams (1974) performed the flow rate–pressure drop measurements for the Natrosol solution. However, unfortunately, they did not provide the values of h, which varied for each flow rate in the experiments. Thus, it is difficult to directly compare their experimental pressure drop data with our theoretical predictions.

6. Concluding remarks

In this work, we have studied the radial flow of a shear-thinning fluid between two disk-shaped plates. Specifically, we applied the lubrication approximation and presented a theoretical framework for calculating the pressure distribution and the flow rate–pressure

drop relation for the Ellis model. We first derived a closed-form expression for the pressure gradient, which allowed us to obtain semi-analytical expressions for the pressure, velocity and $q - \Delta p$ relation for arbitrary values of the Ellis number. We further provided asymptotic expressions for small and large values of El.

To validate the results of our theoretical model, we performed finite-element numerical simulations using the Ellis model for the flow-rate-controlled regime. We found excellent agreement between the velocity, pressure distribution and pressure drop predicted by our theory and those obtained from the numerical simulations. In addition, we studied the entrance length R_{entry} required for the radial velocity of the Ellis fluid to reach its fully developed form. We showed that at small Ellis numbers, the entrance length R_{entry} exhibits only a weak dependence on the shear-thinning characteristics of the fluid and approximates the Newtonian value at low Reynolds numbers. However, at large Ellis numbers, the entrance length may exceed the Newtonian value, depending on the shear-thinning index n_e. Furthermore, we presented a comparison of our theoretical, asymptotic and finite-element simulation results with the experimental measurements of Laurencena & Williams (1974) for the pressure distribution of the Natrosol solution, showing good agreement. However, due to the technological limitations of the experimental system of Laurencena & Williams (1974), new experiments with shear-thinning fluids covering a wider range of shear rates (flow rates) are essential for a more exhaustive comparison with our theoretical results. We believe that such a quantitative comparison is of fundamental importance in non-Newtonian fluid mechanics to evaluate the adequacy of the constitutive model and the accuracy of rheological parameters.

Our theoretical model, based on the Ellis model, captures the interplay between the shear-thinning and zero-shear-rate effects on the pressure distribution and pressure drop, which cannot be modelled using a simple power-law model. This fact emphasises the need for an appropriate constitutive model to accurately describe non-Newtonian flows of shear-thinning fluids.

The presented theoretical approach, employing lubrication theory, extends beyond the Ellis model and can be applied to more complex shear-thinning constitutive models, such as Carreau and Cross, reproducing the high-shear-rate viscosity plateau. However, in contrast to Ellis fluid, for which we derived an explicit governing equation for the pressure gradient (3.9), we expect that no single governing equation can adequately describe the radial flow of Carreau fluid, similar to the case of a straight channel (Boyko & Stone 2021*a*) and capillary (Zhong *et al.* 2022).

Finally, while we analysed here the effect of shear-thinning rheology on hydrodynamic features, it would be interesting to understand how other rheological properties, such as viscoelasticity, influence the pressure distribution and flow rate–pressure drop relation in radial flow. To the best of our knowledge, all previous theoretical studies of the radial flow of viscoelastic fluids considered only small Deborah or Weissenberg numbers, corresponding to weak viscoelasticity (see table 1). Therefore, an interesting future research direction is to study the regime where the viscoelastic behaviour is not a small correction and to consider large Deborah numbers, following the theoretical framework presented recently by Boyko, Hinch & Stone (2024) and Hinch *et al.* (2024) for the flow of an Oldroyd-B fluid in a contraction channel.

Funding. We gratefully acknowledge support by the Israel Science Foundation (Grant No. 1942/23). A.A. acknowledges the support from the Irwin and Joan Jacobs Fellowship. E.B. acknowledges the support from the Israeli Council for Higher Education Yigal Alon Fellowship.

Declaration of interests. The authors report no conflict of interest.

r_i	r_o	h	α	ϵ	η_0	$\tau_{1/2}$	q	El
(mm)	(mm)	(mm)	(–)	(–)	(Pa s)	(Pa)	($m^3\ s^{-1}$)	(–)
5, 10	100	1	0.05, 0.1	0.01	40	8	$1.26 \times 10^{-11} - 1.26 \times 10^{-4}$	$10^{-4} - 10^{3}$

Table 4. Values of the physical parameters used in the finite-element simulations of the Ellis fluid in a radial flow. We consider two values of the shear-thinning index: $n_e = 1.5$ and $n_e = 2.5$. The geometrical parameters ϵ and α are defined as $\epsilon = h/r_o$ and $\alpha = r_i/r_o$. The flow rate q is adjusted to obtain the desired value of the Ellis number El according to (3.10).

Appendix A. Numerical solution of the governing equation

In this appendix, we describe the numerical method used to calculate the pressure distribution $P(R)$ and pressure drop ΔP from (3.12), for given values of El, n_e and α. The method includes two steps. In the first step, we use MATLAB's routine lsqnonlin to find numerically the value of $P'(R)$ for any R value, based on the residual of (3.9). This algorithm is set to converge with residuals below 10^{-6}. In the second step, to calculate $P(R)$ and ΔP from (3.12), we use MATLAB's routine integral, which employs adaptive quadrature to determine the number of points for the discretisation of $P'(R)$, starting from 150 values of R, aiming for a default relative error below 4.9×10^{-6} (see, e.g. Shampine 2008).

Appendix B. Details of finite-element simulations

In this appendix, we describe the numerical techniques used to solve the system of equations (2.1), (2.2) and (2.3). We perform finite-element numerical simulations using COMSOL Multiphysics, which includes the Ellis constitutive model within the laminar flow module (version 6.2, COMSOL AB, Stockholm, Sweden). In our simulations, we use a structured mesh of bilinear elements. The typical mesh consists of approximately 6.5×10^4 elements for $\alpha = 0.05$ and 8.4×10^4 elements for $\alpha = 0.1$. The selected meshes ensure mesh-independent results. For example, in the case of $n_e = 2.5$ and $\alpha = 0.05$, we have a relative error of approximately 0.5 % for up to $El = 25$ between the selected mesh and finer structured mesh of approximately 3.9×10^5 bilinear elements.

We use the axial symmetry of the problem to simplify the three-dimensional configuration into two dimensions and solve the cross-section of the geometry. We impose the no-slip and no-penetration boundary conditions along the walls and fully developed flow with the flow rate q at the entrance of the narrow tube of radius r_i. At the outlet, $r = r_o$, the reference value for the pressure is set to zero. Finally, we calculate the pressure drop between the inlet ($r = r_i$) and outlet ($r = r_o$), and the pressure distribution at the midplane $z = 0$, i.e. $\Delta p = p(r = r_i, z = 0) - p(r = r_o, z = 0)$ and $p(r, z = 0)$.

We summarise in table 4 the values of physical and geometrical parameters used in the numerical simulations. We mainly consider two values of the shear-thinning index, $n_e = 1.5$ and 2.5, and two values of the inlet-to-outlet aspect ratio, $\alpha = r_i/r_o = 0.05$ and 0.1, with the rest of the rheological parameters remaining identical.

As the Ellis model is implicit and requires an initial guess for the viscosity, we choose an initial guess of $\eta_0/100$, ensuring the simulation convergence. Finally, we use the PARDISO solver implemented in COMSOL Multiphysics for simulation and set the relative tolerance of the nonlinear method to 10^{-5}.

Appendix C. Assessing the effect of fluid inertia

Our theory is based on the lubrication approximation, which requires that the aspect ratio $\epsilon = h/r_o$ and the reduced Reynolds number ϵRe are small; that is, $\epsilon \ll 1$ and $\epsilon Re \ll 1$.

As noted in § 3, the reduced Reynolds number ϵRe is the ratio of fluid inertia, $\rho u_c^2/r_o$, to viscous stress, $\eta_c u_c/h^2$, where $u_c = q/2\pi h r_o$ is the characteristic velocity scale and η_c is the characteristic value of viscosity. For a shear-thinning fluid in the small-El (Newtonian) regime, we have $\eta_c \approx \eta_0$, so that $\epsilon Re_{small\ El} = \rho u_c h^2/\eta_0 r_o$. For a shear-thinning fluid in the power-law regime, we have $\eta_c = \eta_0 \mathcal{H}_{power\text{-}law}$, and using (3.11), we obtain $\epsilon Re_{power\text{-}law} = (\rho u_c h^2/\eta_0 r_o) El^{1-(1/n_e)}$ (see also Chun *et al.* 2024).

The effect of fluid inertia is negligible in our simulations, as the reduced Reynolds number ϵRe is vanishingly small. Specifically, using the values from table 4 and estimating the fluid density as $\rho = 10^3$ kg m^{-3}, we find that for $q = 1.26 \times 10^{-9}$ m^3 s^{-1}, corresponding to the small-El regime, $\epsilon Re_{small\ El} = 5 \times 10^{-10}$, while for $q = 1.26 \times 10^{-4}$ m^3 s^{-1} and $n_e = 2.5$, corresponding to the power-law regime with $El = 10^3$, $\epsilon Re_{power\text{-}law} = 3.2 \times 10^{-3}$. Thus, the fluid inertia is indeed negligible in the simulations.

References

Albattat, R. & Hoteit, H. 2021 A semi-analytical approach to model drilling fluid leakage into fractured formation. *Rheol. Acta* **60** (6), 353–370.

Amadou, H., Adler, P.M. & Piau, J.-M. 1978 Converging radial flow of dilute polymer solutions. *J. Non-Newtonian Fluid Mech.* **4**, 229–237.

Ashkenazi, A. & Solav, D. 2025 Parameter certainty quantification in nonlinear models. *Intl J. Engng Sci.* **206**, 104163.

Barmak, I., Picchi, D., Gelfgat, A. & Brauner, N. 2024 Flow of a shear-thinning fluid in a rectangular duct. *Phys. Rev. Fluids* **9** (2), 023303.

Bird, R.B., Armstrong, R.C. & Hassager, O. 1987 *Dynamics of Polymeric Liquids, Volume 1: Fluid Mechanics*, 2nd edn. John Wiley and Sons.

Boyko, E., Hinch, J. & Stone, H.A. 2024 Flow of an Oldroyd-B fluid in a slowly varying contraction: theoretical results for arbitrary values of Deborah number in the ultra-dilute limit. *J. Fluid Mech.* **988**, A10.

Boyko, E. & Stone, H.A. 2021*a* Flow rate–pressure drop relation for shear-thinning fluids in narrow channels: approximate solutions and comparison with experiments. *J. Fluid Mech.* **923**, R5.

Boyko, E. & Stone, H.A. 2021*b* Reciprocal theorem for calculating the flow rate–pressure drop relation for complex fluids in narrow geometries. *Phys. Rev. Fluids* **6**, L081301.

Carreau, P.J. 1972 Rheological equations from molecular network theories. *Trans. Soc. Rheol.* **16** (1), 99–127.

Chatterjee, A. 1993 An infinite series solution for the creeping radial entrance flow of a Newtonian fluid. *AIChE J.* **39** (9), 1563–1568.

Chatterjee, A. 2000 Newtonian radial entrance flow. *AIChE J.* **46** (3), 462–475.

Christov, I.C. 2022 Soft hydraulics: from Newtonian to complex fluid flows through compliant conduits. *J. Phys.: Condens. Matter* **38**, 063001.

Chun, S., Boyko, E., Christov, I.C. & Feng, J. 2024 Flow rate–pressure drop relations for shear-thinning fluids in deformable configurations: theory and experiments. *Phys. Rev. Fluids* **9**, 043302.

Chun, S., Ji, B., Yang, Z., Malik, V.K. & Feng, J. 2022 Experimental observation of a confined bubble moving in shear-thinning fluids. *J. Fluid Mech.* **953**, A12.

Ciriello, V., Lenci, A., Longo, S. & Di Federico, V. 2021 Relaxation-induced flow in a smooth fracture for Ellis rheology. *Adv. Water Resour.* **152**, 103914.

Co, A. 1981 Inelastic flow from a tube into a radial slit. *Ind. Engng Chem. Fundam.* **20** (4), 340–346.

Co, A. & Bird, R.B. 1977 Slow viscoelastic radial flow between parallel disks. *Appl. Sci. Res.* **33**, 385–404.

Co, A. & Stewart, W.E. 1982 Viscoelastic flow from a tube into a radial slit. *AIChE J.* **28** (4), 644–655.

Cross, M.M. 1965 Rheology of non-Newtonian fluids: a new flow equation for pseudoplastic systems. *J. Colloid Sci.* **20** (5), 417–437.

Dai, G. & Bird, R.B. 1981 Radial flow of a Bingham fluid between two fixed circular disks. *J. Non-Newtonian Fluid Mech.* **8** (3–4), 349–355.

Datta, S.S. 2022 Perspectives on viscoelastic flow instabilities and elastic turbulence. *Phys. Rev. Fluids* **7**, 080701.

Ewoldt, R.H. & Saengow, C. 2022 Designing complex fluids. *Annu. Rev. Fluid Mech.* **54**, 413–441.

Gutfinger, C. & Tallmadge, J.A. 1965 Films of non-Newtonian fluids adhering to flat plates. *AIChE J.* **11** (3), 403–413.

HINCH, E.J. 1991 *Perturbation Methods*. Cambridge University Press.
HINCH, J., BOYKO, E. & STONE, H.A. 2024 Fast flow of an Oldroyd-B model fluid through a narrow slowly varying contraction. *J. Fluid Mech.* **988**, A11.
HOUSIADAS, K.D. 2017 Improved convergence based on linear and non-linear transformations at low and high Weissenberg asymptotic analysis. *J. Non-Newtonian Fluid Mech.* **247**, 1–14.
HUTCHINSON, A.J. & WORSTER, M.G. 2025 Fracturing behaviour of a shear-thinning fluid in a lubricated Hele Shaw cell. *J. Fluid Mech.* **1003**, A6.
KHADER, M.S. & VACHON, R.I. 1973 Inertia effects in laminar radial flow of power law fluids. *Intl J. Mech. Sci.* **15** (3), 221–225.
LAURENCENA, B.R. & WILLIAMS, M.C. 1974 Radial flow of non-Newtonian fluids between parallel plates. *Trans. Soc. Rheol.* **18** (3), 331–355.
LEAL, L.G. 2007 *Advanced Transport Phenomena: Fluid Mechanics and Convective Transport Processes*. Cambridge University Press.
LEE, M.C.H. & WILLIAMS, M.C. 1976*a* Radial flow of viscoelastic liquids: part I: theoretical. *J. Non-Newtonian Fluid Mech.* **1** (4), 323–341.
LEE, M.C.H. & WILLIAMS, M.C. 1976*b* Radial flow of viscoelastic liquids: part II: experimental. *J. Non-Newtonian Fluid Mech.* **1** (4), 343–355.
LONGO, S., CHIAPPONI, L., PETROLO, D., BOSA, S. & DI FEDERICO, V. 2022 Ascending non-Newtonian long drops in vertical tubes. *J. Fluid Mech.* **950**, A1.
MATSUHISA, S. & BIRD, R.B. 1965 Analytical and numerical solutions for laminar flow of the non-Newtonian Ellis fluid. *AIChE J.* **11** (4), 588–595.
METER, D.M. & BIRD, R.B. 1964 Tube flow of non-Newtonian polymer solutions: part I. Laminar flow and rheological models. *AIChE J.* **10** (6), 878–881.
MIDDLEMAN, S. 1977 *Fundamentals of Polymer Processing*. McGraw-Hill.
MOUKHTARI, F.E. & LECAMPION, B. 2018 A semi-infinite hydraulic fracture driven by a shear-thinning fluid. *J. Fluid Mech.* **838**, 573–605.
MYERS, T.G. 2005 Application of non-Newtonian models to thin film flow. *Phys. Rev. E* **72** (6), 066302.
NA, T.Y. & HANSEN, A.G. 1967 Radial flow of viscous non-Newtonian fluids between disks. *Intl J. Non-Linear Mech.* **2** (3), 261–273.
ORON, A., DAVIS, S.H. & BANKOFF, S.G. 1997 Long-scale evolution of thin liquid films. *Rev. Mod. Phys.* **69** (3), 931.
PARK, J.M. 2020 Flow classification of radial and squeeze flows between parallel disks. *J. Non-Newtonian Fluid Mech.* **286**, 104416.
PARTAL, P., GUERRERO, A., BERJANO, M., MUÑOZ, J. & GALLEGOS, C. 1994 Flow behaviour and stability of oil-in-water emulsions stabilized by a sucrose palmitate. *J. Texture Studies* **25** (3), 331–348.
PEARSON, J.R.A. 1985 *Mechanics of Polymer Processing*. Elsevier.
PICCHI, D., ULLMANN, A., BRAUNER, N. & POESIO, P. 2021 Motion of a confined bubble in a shear-thinning liquid. *J. Fluid Mech.* **918**, A7.
REINER, M. 1960 *Deformation, Strain, and Flow: an Elementary Introduction to Rheology*. Interscience.
SAYAG, R. & WORSTER, M.G. 2019*a* Instability of radially spreading extensional flows. Part 1. Experimental analysis. *J. Fluid Mech.* **881**, 722–738.
SAYAG, R. & WORSTER, M.G. 2019*b* Instability of radially spreading extensional flows. Part 2. Theoretical analysis. *J. Fluid Mech.* **881**, 739–771.
SCHWARZ, W.H. & BRUCE, C. 1969 The radial flow viscometer. *Chem. Engng Sci.* **24** (2), 399–413.
SHAMPINE, L.F. 2008 Vectorized adaptive quadrature in MATLAB. *J. Comput. Appl. Maths* **211** (2), 131–140.
SHAMU, T.J., ZOU, L., KOTZÉ, R., WIKLUND, J. & HÅKANSSON, U. 2020 Radial flow velocity profiles of a yield stress fluid between smooth parallel disks. *Rheol. Acta* **59** (4), 239–254.
SHENDE, T., NIASAR, V.J. & BABAEI, M. 2021 Effective viscosity and Reynolds number of non-Newtonian fluids using Meter model. *Rheol. Acta* **60** (1), 11–21.
SISKO, A.W. 1958 The flow of lubricating greases. *Ind. Engng Chem.* **50** (12), 1789–1792.
STEINIK, C., PICCHI, D., LAVALLE, G. & POESIO, P. 2024 Capillary imbibition of shear-thinning fluids: From Lucas–Washburn to oscillatory regimes. *Phys. Rev. Fluids* **9** (2), 023305.
STELLER, R.T. 2001 Generalized slit flow of an Ellis fluid. *Polym. Engng Sci.* **41**, 1859–1870.
TADMOR, Z. & GOGOS, C.G. 2013 *Principles of Polymer Processing*. John Wiley and Sons.
ZHONG, X., MITRA, H., VEILLEUX, J.-C., SIMMONS, E., SHI, G.H. & ARDEKANI, A.M. 2022 The role of liquid rheological properties on the injection process of a spring-driven autoinjector. *Intl J. Pharm.* **628**, 122296.
ZOU, L., HÅKANSSON, U. & CVETKOVIC, V. 2020 Radial propagation of yield-power-law grouts into water-saturated homogeneous fractures. *Intl J. Rock Mech. Mining Sci.* **130**, 104308.